Author Manuscript

Author Manuscript

Author Manuscript

Author Manuscript

HHS Public Access

Author manuscript

Concepts Magn Reson Part B Magn Reson Eng. Author manuscript; available in PMC 2016 October 27.

Published in final edited form as:

Concepts Magn Reson Part B Magn Reson Eng. 2016 February ; 46(1): 25–40. doi:10.1002/cmr.b.21319.

Dependence of B1+ and B1− Field Patterns of Surface Coils on the Electrical Properties of the Sample and the MR Operating Frequency

Manushka V. Vaidya[1,2,3], **Christopher M. Collins**[1,2,3], **Daniel K. Sodickson**[1,2,3], **Ryan Brown**[1,3], **Graham C. Wiggins**[1], and **Riccardo Lattanzi**[1,2,3]

[1]Department of Radiology, Center for Advanced Imaging Innovation and Research (CAI^{2}R) and Bernard and Irene Schwartz Center for Biomedical Imaging, New York University School of Medicine, New York, NY 10016

[2]The Sackler Institute of Graduate Biomedical Sciences, New York University School of Medicine, New York, NY 10016

[3]NYU WIRELESS, Polytechnic Institute of New York University, Brooklyn, NY 11201

Abstract

In high field MRI, the spatial distribution of the radiofrequency magnetic ($\boldsymbol{B}_1$) field is usually affected by the presence of the sample. For hardware design and to aid interpretation of experimental results, it is important both to anticipate and to accurately simulate the behavior of these fields. Fields generated by a radiofrequency surface coil were simulated using dyadic Green's functions, or experimentally measured over a range of frequencies inside an object whose electrical properties were varied to illustrate a variety of transmit (B_1^+) and receive (B_1^-) field patterns. In this work, we examine how changes in polarization of the field and interference of propagating waves in an object can affect the $\boldsymbol{B}_1$ spatial distribution. Results are explained conceptually using Maxwell's equations and intuitive illustrations. We demonstrate that the electrical conductivity alters the spatial distribution of distinct polarized components of the field, causing "twisted" transmit and receive field patterns, and asymmetries between $|B_1^+$ and $|B_1^-$. Additionally, interference patterns due to wavelength effects are observed at high field in samples with high relative permittivity and near-zero conductivity, but are not present in lossy samples due to the attenuation of propagating EM fields. This work provides a conceptual framework for understanding $\boldsymbol{B}_1$ spatial distributions for surface coils and can provide guidance for RF engineers.

Keywords

magnetic resonance imaging; MRI; B1 field patterns; B1 twisting; electrical properties; interference patterns; dyadic Green's functions; electromagnetic field simulations; high-field MRI

Correspondence to: Manushka Vaidya; manushka.vaidya@med.nyu.edu.

Author Manuscript Author Manuscript Author Manuscript Author Manuscript

INTRODUCTION

The spatial distribution of the radiofrequency (RF) magnetic field ($\boldsymbol{B}_1$) is affected by the operating frequency of the MR scanner (1–5), the electrical properties (i.e. permittivity and conductivity) of the body, and the body geometry (6,7). This, for example, can result in the distinctive "twisting" asymmetry of the receive (B_1^-) and transmit (B_1^+) fields observed at high magnetic field strength (8,9), and/or in complex interference patterns (2,3,7,10–13). Many prior studies have demonstrated and analyzed $\boldsymbol{B}_1$ field pattern variations in simulations and experiments (1–16); therefore, all references cited are selected example publications. In this work we offer a comprehensive description of these phenomena occurring as a consequence of a) $\boldsymbol{B}_1$ polarization effects and b) the interaction between propagating waves.

Previous studies have shown that for MRI at ultra high field (UHF) (i.e., static magnetic field amplitude $B_0 \geq 7$T), propagation of waves from different directions (either from different sources or incident and reflected waves) can cause interferences within the object (12,13), since the wave-length of the electromagnetic (EM) field at UHF is comparable to the dimensions of the imaged object. These interference patterns can cause signal inhomogeneities, which compromise image contrast and signal-to-noise ratio (SNR), and which also may present safety concerns, because of local regions of high electric ($\boldsymbol{E}$) field (2,3,7,10–13). For example, interference patterns that are formed because of fields propagating from multiple current elements around the sample can result in the center-bright effect (13,14) on MR images, which is often seen in deep regions of the brain at 7 T (15). Local regions of low signal observed in UHF body MRI (16) represent another example of interference patterns. Possible strategies to mitigate signal inhomogeneity include RF shimming (4,17,18) and parallel transmission (19–21). Gaining a better understanding of these phenomena may lead to alternative solutions to reduce image inhomogeneity.

The $\boldsymbol{B}_1$ field patterns depend not only on the operating frequency, but also on the sample's electrical properties and geometry. Glover et al. (1) demonstrated that the $\boldsymbol{B}_1$ field for a volume coil exhibits greater spatial variation in the radial direction as the sample's relative permittivity increases, owing to the shorter wavelength of the propagating EM field. On the other hand, increasing the conductivity of the sample resulted in inhomogeneous field patterns caused by eddy currents. It was also shown that the spatial field distribution changes with the size of the object, since interference patterns vary if the boundaries of the sample are further away from the source. Work by Yang et al. (12) demonstrated that interference pattern behavior depends on the electrical properties of the sample; standing wave patterns in low-conductivity water samples excited by a single surface coil were not present in more conductive samples, and the interference pattern observed for conductive samples was a consequence of decaying traveling waves in the forward and reflected directions.

RF coils are often differentiated by the polarization of their current drive scheme (e.g. circularly-polarized versus linearly-polarized drives). However, the sample's properties can change the polarization within the sample and influence the resulting spatial pattern of transmit and receive sensitivity. In the early 1980s, it was established that exciting a volume coil in quadrature could produce a nearly circularly-polarized field, and this improved image

Author Manuscript Author Manuscript Author Manuscript Author Manuscript

uniformity (1), increased SNR and reduced SAR (22). A surface loop coil, on the other hand, can only be driven to produce a linearly polarized field in free space. Induced currents, however, which depend on the electrical properties of the sample, can modify the otherwise linearly polarized field of a surface loop coil and produce an elliptically polarized field (8,23,24). It is therefore important to understand and anticipate these effects on the $\boldsymbol{B}_1$ spatial distribution, especially for RF coil development at UHF, where these effects are more evident. Our work further investigates the particular effects of conductivity and permittivity on the polarized components of the $\boldsymbol{B}_1$ field.

The overall objective of the current work is to present a comprehensive conceptual framework based on Maxwell's equations to investigate and explain the spatial distribution of $\boldsymbol{B}_1$ within a dielectric sample near a surface coil. Our work demonstrates that the electrical properties of the sample and the operating frequency affect both the polarization and the propagation of the $\boldsymbol{B}_1$ field in the imaged object, and these effects dictate the spatial distribution of the transmit and receive field. Computer simulations and experimental measurements are utilized to augment understanding of field behavior observed in both routine MRI examinations and more extreme conditions. Preliminary results of this work were presented at the Annual Meeting of the International Society for Magnetic Resonance in Medicine in Melbourne (Australia) in 2012 (25).

THEORY

The harmonic time varying magnetic field generated by an RF coil, and the associated electric field, can be written as

$$\boldsymbol{B}_1(\boldsymbol{r},t)=\boldsymbol{B}_1(\boldsymbol{r})e^{i\omega t} \quad [1]$$

$$\boldsymbol{E}(\boldsymbol{r},t)=\boldsymbol{E}(\boldsymbol{r})e^{i\omega t} \quad [2]$$

where using phasor notation, $\boldsymbol{B}_1$ can be decomposed into complex components along the orthogonal x, y, and z axes of a laboratory frame: B_{1x}, B_{1y}, and B_{1z}. $i=\sqrt{-1}$ is the imaginary unit. The Larmor frequency (f_0) is defined as follows:

$$f_0=\omega/2\pi=\gamma\boldsymbol{B}_0 \quad [3]$$

Here γ is the gyromagnetic ratio and $\boldsymbol{B}_0$ is the static magnetic field strength.

If we define $\boldsymbol{B}_0$ to be parallel to the z axis, the B_{1z} component does not take part in the excitation of spins (23). The vector norm of full and transverse $\boldsymbol{B}_1$ fields are defined as

$$\|\boldsymbol{B}_1\|=\sqrt{B_{1x}B_{1x}^*+B_{1y}B_{1y}^*+B_{1z}B_{1z}^*} \quad [4]$$

Author Manuscript Author Manuscript Author Manuscript Author Manuscript

$$\|\boldsymbol{B}_{1xy}\| = \sqrt{B_{1x}B_{1x}^{*} + B_{1y}B_{1y}^{*}} \quad [5]$$

Transmit and Receive Magnetic Fields

A number of authors have used a variety of methods to show that, for a given coil, the circularly-polarized component rotating in the same direction as nuclear precession is pertinent in nuclear excitation, and the circularly polarized component rotating opposite to the direction of nuclear precession is pertinent in signal reception (1,23,26–29). Let us define the transmit field generated by an RF coil as the $\boldsymbol{B}_1$ field in the positively rotating frame of reference $(\tilde{B}_1^{+})$, which can be derived, as shown by Hoult (23), in terms of the x and y components of the $\boldsymbol{B}_1$ field in the laboratory frame of reference:

$$\tilde{B}_1^{+} = \frac{(B_{1x} + iB_{1y})}{2} \quad [6]$$

$\tilde{B}_1^{+}$ is assumed to be rotating in the same direction as nuclear precession. Here the tilde (~) indicates fields in a rotating frame of reference. The $\boldsymbol{B}_1$ field in the negatively rotating frame $(\tilde{B}_1^{-})$ can be derived as (23)

$$\tilde{B}_1^{-} = \frac{(B_{1x} - iB_{1y})^{*}}{2} = \frac{(B_{1x}^{*} + iB_{1y}^{*})}{2} \quad [7]$$

Some authors have used an alternative formulation of the receive field without the complex conjugation sign (28,30). While the amplitude of $\tilde{B}_1^{-}$ is identical for both definitions, the phase is different (see Appendix).

B_{1x} or B_{1y} can be considered to consist of two counter-rotating components, each with amplitude $|B_{1x}|/2$ or $|B_{1y}|/2$, which at any instant in time can be added together to form the full amplitude of $|B_{1x}|$ or $|B_{1y}|$ [Figs. 1(A,B)]. Since only one component rotates in the direction of nuclear precession, the normalization factor 2 is needed in Eqs. [6] and [7] (1,23). As B_{1x} and B_{1y} are in general both complex, Eqs. [6] and [7] are not equivalent. Hoult's work demonstrated that the sensitivity of an RF coil to MR signal, as a function of position, is proportional to the complex conjugate of $\tilde{B}_1^{-}$, if the transmit field is given by Eq. [6]. For convenience, we will hereafter refer to the signal sensitivity distribution as the "receive field," even though it does not necessarily match the field generated by any particular driven coil or precessing spin—it is instead a construct designed to describe the RF sensitivity distribution succinctly via the principle of reciprocity.

Importantly, the definitions for the transmit and receive fields depend on the orientation of the $\boldsymbol{B}_0$ field. Technically, Eq. [6] is associated with excitation and Eq. [7] with reception only if the $\boldsymbol{B}_0$ is oriented in the negative z direction. If, however, $\boldsymbol{B}_0$ is oriented in the positive z direction, the direction of nuclear precession would change and the equations for transmit

Author Manuscript Author Manuscript Author Manuscript Author Manuscript

and the receive fields would be interchanged, i.e., the transmit field would correspond to Eq. [7] and the receive field would correspond to Eq. [6].

Circular Polarization

The vector orientation of a time-varying magnetic field in the transverse plane, i.e., its polarization, depends on the amplitude of the two pertinent perpendicular components and their phase difference (31). An EM field is circularly polarized if, for a given frequency, these two perpendicular components are equal in amplitude and 90 degrees out of phase. In fact, over time the summation vector of the two components describes a circular locus on a plane defined by the axes of the components (e.g. on a plane at a fixed z if the components are along x and y). If both components have nonzero amplitudes and the field is neither linearly polarized (with the phase difference of the orthogonal time-varying components being equal to either 0 or 180 degrees), nor circularly-polarized (with the components having equal magnitudes and a phase difference of +90 or −90 degrees), the field is said to be elliptically polarized (31).

The $\boldsymbol{B}_1$ field of an RF coil in the transverse plane is said to be circularly polarized about the z-axis if the two perpendicular sinusoidal time varying components, B_{1x} and B_{1y}, obey the above conditions. For example, in a volume coil, circular polarization can be achieved by quadrature excitation, i.e., using two coils producing linearly-polarized fields that are physically orthogonal and exciting one of the coils with a phase lag of 90 degrees with respect to the other. The circularly polarized $\boldsymbol{B}_1$ field can be distinguished further as right circularly polarized or left circularly polarized, depending on the relative orientation of the B_{1x} and B_{1y} components. If $\tilde{B}_1^+$, i.e. the transmit field, is defined as the right (counter-clockwise) circularly polarized component of the $\boldsymbol{B}_1$ field, then $\tilde{B}_1^-$, i.e. the receive field, is the left (clockwise) circularly polarized component. The opposite polarization of the pertinent field components during transmission and reception in MR has been proven mathematically and graphically in various ways (1,23,27,32). An alternative illustration of the relationship between $\tilde{B}_1^+$ and $\tilde{B}_1^-$ is shown in Fig. 2. The figure shows that since the direction of propagation in transmission (from the coil to the sample) is opposite to that in reception (from the sample to the coil), the "handedness" of the transmit and receive fields must be opposite as well in order to follow the direction of nuclear precession in both cases.

Relationship between |B1+| and |B1−|

For a single surface loop coil, we can use the following relations (23):

$$B_{1x}=KI_{\mathrm{o}}C_{\mathrm{ox}}e^{i(\phi+\alpha)} \quad [8]$$

$$B_{1y}=KI_{\mathrm{o}}C_{\mathrm{oy}}e^{i(\phi+\beta)} \quad [9]$$

Author Manuscript Author Manuscript Author Manuscript Author Manuscript

Here, I_0 and ϕ are the amplitude and phase of the current in the coil, K is a coil-geometry-dependent scaling factor, C_{ox} and C_{oy} are frequency- and position-dependent attenuation factors, and α and β are the position- and frequency-dependent phase changes produced by the field propagation and by perturbations in the sample.

From here onwards, for simplicity, the transmit and receive $\boldsymbol{B}_1$ field will be denoted without a tilde as B_1^+ and B_1^-, respectively, though the definitions in Eqs. [6] and [7] will continue to apply. Let us now compare the amplitude of B_1^+ and B_1^- by substituting Eqs. [8] and [9] in Eqs. [6] and [7]:

$$|B_1^{\pm}|=\frac{KI_o}{2}\sqrt{\begin{array}{c}(C_{0x}\cos(\phi+\alpha))^2+(C_{0y}\sin(\phi+\beta))^2\mp 2C_{ox}C_{oy}\cos(\phi+\alpha)\sin(\phi+\beta)\\+(C_{0x}\sin(\phi+\alpha))^2+(C_{0y}\cos(\phi+\beta))^2\pm 2C_{ox}C_{oy}\sin(\phi+\alpha)\cos(\phi+\beta)\end{array}}$$
$$=\frac{KI_o}{2}\sqrt{{C_{0x}}^2+{C_{oy}}^2\mp 2C_{ox}C_{oy}\cos(\phi+\alpha)\sin(\phi+\beta)\pm 2C_{ox}C_{oy}\sin(\phi+\alpha)\cos(\phi+\beta)}$$

[10]

The only difference between the amplitude of the transmit and receive fields is the sign of the third and sixth term in the sum under the square root. Note that if propagation-related and sample-induced phase changes are negligible (i.e., α and β both approach 0), then the transmit and receive field amplitudes are equal to half the magnitude of the transverse component of $\boldsymbol{B}_1$:

$$\|\boldsymbol{B}_{1xy}\|=2|B_1^+|=2|B_1^-|=KI_o\sqrt{{C_{ox}}^2+{C_{oy}}^2} \quad [11]$$

In other words, if the phase changes are negligible, the $\boldsymbol{B}_1$ field of a surface coil is linearly polarized and equally decomposes into right and left circularly polarized components [Figs. 1(A,B)].

Effect of Electrical Conductivity on |B1+| and |B1−|

The fields in Eqs. [1] and [2] obey Faraday's law of induction and the modified Ampere's law:

$$\nabla\times\boldsymbol{E}=-i\omega B_1 \quad [12]$$

$$\nabla\times\boldsymbol{B}_1=\mu_0(\sigma+i\omega\varepsilon_r\varepsilon_0)\mathbf{E} \quad [13]$$

Here, μ_0 is the magnetic permeability of free space, σ and ε_r are the location-dependent electrical conductivity and relative permittivity, and ε_0 is the permittivity of free space.

Author Manuscript Author Manuscript Author Manuscript Author Manuscript

Faraday's law (Eq. [12]) shows that the coil's $\boldsymbol{B}_1$ field induces an $\boldsymbol{E}$ field that is 90° out-of-phase with $\boldsymbol{B}_1$, indicated by the multiplicative factor i. The modified Ampere's law (Eq. [13]) indicates that both displacement currents ($i\omega\varepsilon_0\varepsilon_r\boldsymbol{E}$) and conduction currents ($\sigma\boldsymbol{E}$) associated with the electric field contribute to the overall magnetic field in the sample. As stated in the previous section, we expect a single surface coil in free space to produce a linearly-polarized field through-out space. Since the induced $\boldsymbol{E}$ field and the $\boldsymbol{B}_1$ field from the coil are 90° out of phase (Eq. [12]), the magnetic field induced by the conduction currents in a conductive sample (Eq. [13]) adds out-of-phase contributions with location-dependent orientation to the overall $\boldsymbol{B}_1$, and therefore affects its polarization such that it can become elliptical. On the other hand, the displacement currents, due to the additional factor of i in Eq. [13], induce a magnetic field that is back in phase with the original $\boldsymbol{B}_1$ field, and therefore can add only in-phase contributions to the overall $\boldsymbol{B}_1$ field within the sample, which may affect the orientation of the linearly-polarized field, but cannot change its linearly-polarized nature.

While a linearly-polarized $\boldsymbol{B}_1$ field may be decomposed into equal contributions of right (B_1^+) and left (B_1^-) circular polarization (1,11) [Figs. 1(A,B)], a field that is elliptically-polarized will have a larger contribution of one or the other at any given position in the sample [Figs. 1(C,D)]. The interaction between the original $\boldsymbol{B}_1$ produced by the current in the coil and the magnetic field generated by the conduction currents induced in the sample result in a net elliptically-polarized $\boldsymbol{B}_1$ within the sample that is preferentially right circularly polarized near one side of the coil and left circularly polarized near the other side, for the case of a surface loop coil (8,27,33). Therefore, a larger-amplitude right circularly polarized component will be present on one side of the coil, and a smaller-amplitude right circularly polarized component will be present on the other side of the coil. The distribution of the left circularly-polarized component, meanwhile, will mirror that of the right circularly-polarized component. As $|B_1^+$ and $|B_1^-$ maps only show contributions from the right or the left circularly-polarized component, respectively, the maps appear asymmetric with two characteristic lobes, one larger than the other, because of the relative amplitude of right vs. left circularly-polarized component. This is the origin of the asymmetric "twisting" of B_1^+ and B_1^-, which is observed especially at high magnetic field strength (8,25). Note that, although the $|B_1^+$ and $|B_1^-$ maps for a surface coil near a symmetric sample are mirror images of each other in the transverse plane (i.e., the positions of the two lobes are reversed), the $\|\boldsymbol{B}_1\|$ map, which includes contributions from both right and left circular polarization, as well as the B_{1z} component, is perfectly symmetric with respect to the coil.

Dependence of |B1+| and |B1−| on MR Operating Frequency

The $|B_1^+$ or $|B_1^-$ spatial field distributions show greater asymmetry at higher main magnetic field strengths (9). A larger $\boldsymbol{B}_0$ (i.e., a larger operating Larmor frequency) requires a larger ω for imaging a given nucleus (Eq. [3]), such that a given $\boldsymbol{B}_1$ field will induce a larger $\boldsymbol{E}$ field (Faraday's law (Eq. [12])). As a consequence, from the modified Ampere's law (Eq. [13]), assuming sample conductivity is either frequency-independent or increases with frequency (as it does in tissue), the conduction currents induced in the sample are larger and produce larger out-of-phase contributions to the $\boldsymbol{B}_1$ field, resulting in more pronounced asymmetries

Author Manuscript Author Manuscript Author Manuscript Author Manuscript

in the spatial distribution of the transmit and receive fields of a surface coil. On the other hand, at decreasing field strengths, the induced conduction currents become smaller and result in smaller out-of-phase contributions to the $\boldsymbol{B}_1$ field. As a consequence, and given smaller contributions to phase from field propagation effects as well, α and β in Eq. [10] approach zero. Therefore, as $\boldsymbol{B}_0$ is reduced, the $\boldsymbol{B}_1$ field of a surface coil becomes more linearly polarized, and $|B_1^+$ and $|B_1^-$ become more symmetric (Eq. [11]).

Interference Patterns in |B1+| and |B1−|

The wavelength (λ) and the skin depth (δ) for a plane wave propagating inside a material can be calculated from the following equations (31):

$$\lambda=\frac{2\pi}{\omega}\left[\frac{\mu\varepsilon_0\varepsilon_r}{2}\left(\sqrt{1+\left(\frac{\sigma}{\varepsilon_0\varepsilon_r\omega}\right)^2}+1\right)\right]^{-1/2} \quad [14]$$

$$\delta=\frac{1}{\omega}\left[\frac{\mu\varepsilon_0\varepsilon_r}{2}\left(\sqrt{1+\left(\frac{\sigma}{\varepsilon_0\varepsilon_r\omega}\right)^2}-1\right)\right]^{-1/2} \quad [15]$$

Note that the electrical properties of a sample depend on the frequency, and therefore are different for the same tissue when probed at frequencies corresponding to different $\boldsymbol{B}_0$ field strengths (34).

Wavelength effects and interference patterns can be observed in $|B_1^+$ and $|B_1^-$ when the propagating fields interact with the dielectric sample. This effect, for example, can be responsible for signal inhomogeneities and local regions of high SAR in UHF MRI (2,3,7,10–13), where the wavelength of the EM field is smaller than typical body dimensions. As a rule of thumb, for a single surface coil, interference patterns in $|B_1^+$ and $|B_1^-$ are possible if one half-wavelength of the EM field inside the object is smaller than the diameter of the object, and the skin depth, which determines how far an EM wave can propagate, is sufficiently large, so that the EM field can reflect from boundaries far from a surface coil, or can interfere within the sample when propagating from multiple coils. Samples with high conductivity correspond to a small skin depth (Eq. [15]) and less field interference is expected within them, since the forward wave is attenuated substantially before reflecting off object boundaries or interfering with fields from other sources. The forward wave is not required to reach the far boundary of the object to generate interference patterns for cases with multiple coil elements, as the fields from individual coil elements in the array can interact with each other without any substantial reflection at boundaries. The center-bright effect, for example, is observed in MR images acquired using volume coils or multi-element arrays driven in a quadrature-type phase arrangement (13,14). With appropriate phased transmission, the location of the interference can be changed or made

Author Manuscript Author Manuscript Author Manuscript Author Manuscript

less singular (potentially improving field homogeneity), but similar flexibility is not possible with single coil excitations.

From Eq. [14], when $\varepsilon_r\varepsilon_0\omega \gg \sigma$, the wavelength is inversely proportional to the square root of the relative permittivity:

$$\lambda \propto 1/\sqrt{\varepsilon_r} \quad [16]$$

Therefore, for high values of relative permittivity, the wavelength can be sufficiently short to cause interference patterns even at relatively low field strengths.

Note that EM field interference can occur without dielectric resonance. Dielectric resonances occur at very specific frequencies when the sample conductivity is very low, often when wavelengths are some particular fraction of some dimension of the dielectric sample, allowing for a characteristic standing wave pattern. They are characterized by a relatively large frequency-specific response to a given stimulus, e.g., a $\boldsymbol{B}_1$ field at or near the natural frequency of the sample (13). While interference patterns can be observed at any frequency, dielectric resonances occur only when the frequency of the EM field matches the natural resonant frequency of the sample.

METHODS

Experiments

In order to demonstrate an unusual $|B_1^+$ field pattern, as well as to validate our simulations, we experimentally measured B_1^+ maps generated by a transmit-receive coil in two 26.7 liter cylindrical water phantoms (diameter = 29.7 cm and length = 38.5 cm) doped with 10.7 and 52.1 g of NaCl (99%, Sigma-Aldrich), respectively. The corresponding phantom conductivities were σ = 0.12 and 0.41 S/m, respectively, at 297.2 MHz (measured using 85070E Dielectric Probe Kit, Agilent Technologies). A 10 × 10 cm transmit-receive window coil was constructed and mounted 1.4 cm from the phantom. The coil was tuned and matched separately for both saline solutions (S_{11} at 297.2 MHz < −23 dB). This setup was mimicked in an in-house full-wave simulation framework based on dyadic Green's functions (DGF) (30). Experimental and simulation set-up is shown in the bottom row of Fig. 3. Experiments were carried out on a Siemens whole-body 7 T scanner (MAGNE-TOM, Erlangen, Germany). Flip-angle maps were obtained using a turbo-FLASH-based technique (35) and converted to Tesla for input of 1 V, based on sequence parameters and system characteristics:

$$B_1 = \frac{\alpha}{2\pi\gamma V_{\mathrm{ref}} T_{\mathrm{ref}} \left(\frac{\alpha_{\mathrm{nom}}}{\alpha_{\mathrm{ref}}}\right)}. \quad [17]$$

Here, α is the flip angle map in degrees, γ is the gyromagnetic ratio, V_{ref} is the transmit voltage required to achieve a 180° flip angle (α_{ref}), T_{ref} is the time duration of the reference pulse, which was 1 ms, and α_{nom} is the nominal flip angle.

Author Manuscript Author Manuscript Author Manuscript Author Manuscript

Simulations

The DGF simulation framework (30) was used to calculate the EM field generated inside a uniform cylindrical sample by a transmit-receive cylindrical window coil (Fig. 4) for a variety of main magnetic field strengths and object electrical properties. In all cases, the EM field was calculated at the proton resonance frequency in the transverse plane through the center of the dielectric cylinder, which was aligned with the center of the coil (Fig. 4). The phase distribution inside the sample was calculated using a 2D Goldstein branch cut phase unwrapping algorithm (36,37) with the location on the sample nearest the center of the coil defined as having phase of 0 in all cases. All amplitude and phase images were generated with a matrix size of 42 × 42, corresponding to a resolution of 0.73 × 0.73 cm^2. All images were then interpolated either by a factor of two (Figs. 5–9) for improved display, or by a factor of three to match experimental results (Fig. 3).

The conductive shield of the MR system was modeled at a distance of 34.25 cm from the axis of the cylinder. The coil was modeled with copper conductors with electrical conductivity equal to 5.8×10^7 S/m and thickness equal to the skin depth at the operating frequency associated with each magnetic field strength. Calculations were implemented in MATLAB (MathWorks, Natick, MA) and *m* and *n*, which are the longitudinal and the radial expansion coefficients, respectively (30,38), were varied from −50 to +50 and from −40 to +40 with unit step, corresponding to a total of 16,362 modes, to ensure convergence of the calculations.

RESULTS

Figure 3 shows an example of an unusual $\boldsymbol{B}_1$ field pattern seen in experiment and simulation. For the phantom with $\sigma = 0.12$ S/m, both transmit and receive field patterns exhibit numerous nulls and high intensity regions, due to destructive and constructive interferences between forward and reflected waves. Results from experiments and simulations are in excellent agreement. For a sample with higher conductivity ($\sigma = 0.41$ S/m), however, the fields can no longer propagate across the sample and back; therefore, the interference pattern is not formed and the fields monotonically decrease with distance from the coil [Figs. 3(D,E)]. While for both cases the wavelength is shorter than the diameter of the phantom, interferences are present only in the phantom whose low conductivity corresponds to skin depth larger than the diameter [Figs. 3(A,B)].

The coil/phantom set-up used for the remaining simulations is illustrated in Fig. 4. Figure 5 shows that in the case of a conductive sample ($\sigma = 0.69$ S/m) at 1.5 T, both $|B_1^+$ and $|B_1^-$ are asymmetric with respect to the center of the coil and exhibit mirror-image asymmetries [Figs. 5(A,B)]. As expected from the theory, if the sample is nonconductive ($\sigma \approx 0$ S/m), there are no induced conductive currents that affect the phase of the $\boldsymbol{B}_1$ field, so $|B_1^+$ and $|B_1^-$ are identical and symmetric with respect to the coil [Eq. [11] and Figs. 5(D,E)]. The spatial distribution of the magnitude of the full $\boldsymbol{B}_1$ field is always symmetric with respect to the surface coil [Figs. 5(C,F)] showing more attenuation in the case of the lossy sample [Fig. 5(C)]. Figure 6 shows that the phase distributions of B_1^+ and B_1^- are homogenous for the non-conductive sample [Figs. 6(D–F)], but the phase of B_1^- depends on the definition used

Author Manuscript Author Manuscript Author Manuscript Author Manuscript

for calculating the receive field (see also Appendix). Asymmetries in the transmit field distribution (mirrored in the receive field, results not shown) are more pronounced for larger main magnetic field strength [Figs. 7(A–D)], because larger conductive currents and shorter wavelengths in the sample result in more significant phase changes [Figs. 7(E–H)]. Figure 8 shows that for a nonconductive cylindrical sample with 30.6 cm diameter, wavelength effects at 7 T cause interference patterns between forward and reflected waves even when the sample permittivity is small. These effects become more evident as the permittivity is increased [Figs. 8(B–E)], because of the inverse relationship between the square root of the permittivity and wavelength (Eq. [16]). At 0.2 T, on the other hand, for the same sample geometry and conductivity, a significantly higher relative permittivity is required for the wave-length to be sufficiently short to cause interference patterns [Fig. 8(J)]. For an object with near zero conductivity and relative permittivity approximately equal to that of distilled water ($\varepsilon_r = 79$, $\sigma = 10^{-6}$ S/m), $|B_1^+$ and $|B_1^-$ are each approximately half of $\|\boldsymbol{B}_{1xy}\|$ (Eq. [11]) at both 0.2 T and 7 T [Figs. 9(A,B,E,F)]. For a conductive sample ($\varepsilon_r = 79$, $\sigma = 0.5$ S/m), similar results are observed at low field [Figs. 9(C,D)], but at 7 T the spatial distributions of the transmit and receive fields are neither uniform nor equal to half of $\|\boldsymbol{B}_{1xy}\|$ throughout the sample except for a few locations [Figs. 9(G,H)], due to the effect of conduction currents. The results indicate that $|B_1^+$ and $|B_1^-$ are approximately half of $\|\boldsymbol{B}_{1xy}\|$ only if conduction currents within the sample are negligible, even in the presence of substantial displacement currents.

DISCUSSION

The transmit and receive field patterns depend on the polarization of the $\boldsymbol{B}_1$ field and its spatial distribution within the sample. Assuming that the $\boldsymbol{B}_0$ field is oriented along the negative z direction, a $|B_1^+$ map shows only the right circularly polarized component of $\boldsymbol{B}_1$, whereas a $|B_1^-$ map shows only the left circularly polarized contribution. The polarization of the $\boldsymbol{B}_1$ field in the sample associated with a surface loop coil depends on the operating frequency and the sample's electrical properties. At low frequencies, the phase changes caused by the sample are negligible and $\boldsymbol{B}_1$ remains preferentially linearly polarized; therefore, the field of a single surface coil can be divided nearly equally into right and left circularly polarized components (Fig. 1), resulting in identical $|B_1^+$ and $|B_1^-$ maps (Eq. [11], Figs. 5 and 9). At high frequencies, however, conduction currents induced in the sample generate larger out-of-phase contributions that can change the polarization of $\boldsymbol{B}_1$ and its spatial distribution, resulting in asymmetric $|B_1^+$ and $|B_1^-$ maps that "twist" towards different sides of the coil, and are mirror images of each other [Figs. 5(A,B)] (27,32,33). Full $\|\boldsymbol{B}_1\|$ maps, however, contain both the right and left circularly polarized components as well as the B_{1z} component, and are symmetric with respect to the center of the coil for both conductive and nonconductive samples [Figs. 5(C,F)].

Up to this point, though we have described the effects of $\boldsymbol{B}_1$ polarization changes in the sample, we have not offered any intuitive means (apart from electrodynamic simulations) to predict the particular distribution of elliptical polarization for a given coil and sample geometry. In Fig. 10, we illustrate an "effective mirror current" construct (33), which we

Author Manuscript Author Manuscript Author Manuscript Author Manuscript

have found to be useful for predicting $\boldsymbol{B}_1$ polarization distributions. Current passing through a surface coil in air ($\varepsilon_r = 1$, $\sigma = 0$) induces a familiar magnetic field (modified Ampere's law), which is linearly polarized. If the coil is placed above a conductive sample, it induces an "effective mirror current" distribution in the sample (Faraday's law). (Note that the mirror current in Fig. 10 is shown for simplicity as a discrete loop, whereas currents induced in an actual sample would be more distributed, while sharing the same general shape.) This "effective mirror current" then induces its own circulating magnetic field (modified Ampere's law). The direction of the two interacting magnetic fields can be determined from the right hand rule (i.e., with the thumb in the direction of the current the curled fingers depict the direction of the induced magnetic field). The field components associated with the mirror current have both an orientation and a phase that are different from those of the field components associated with the driving current. As a result, elliptical polarization is generated in the sample. As shown in the figure, the orientations are such that right circular polarization dominates on one side of the coil, while left circular polarization dominates on the other. This simple "effective mirror current" model explains how a single coil, as opposed to two distinct surface coils that are spatially and temporally offset, can produce spatially varying elliptical polarization in the presence of a conductive sample. A previous schematic by Wardenier also attributed the asymmetry of the transmit and receive field to the spatial distribution of elliptically polarized $\boldsymbol{B}_1$ field (8), but it did not explain the spatial distribution of conduction or eddy currents.

The fact that $|B_1^+$ and $|B_1^-$ exhibit mirror image asymmetries does not indicate that the principle of reciprocity does not hold at high field strengths. In fact, while the principle of reciprocity in an NMR context was first proposed at lower field strengths (39), at which the transmit and receive fields are more similar, Hoult's work in 2000 demonstrated that this fundamental principle of electromagnetics is still valid at higher field strengths (23). In fact, in simulations the principle of reciprocity is applied every time they receive sensitivity of an RF coil is calculated from the fields produced by driving the same RF coil.

As shown in Figs. 5 and 6 and explained with Eqs. [12] and [13], the conductivity of the sample rather than the permittivity is responsible for asymmetries in circularly polarized components in $\boldsymbol{B}_1$. The conduction currents (i.e., $\sigma\boldsymbol{E}$) introduce out-of-phase contributions to $\boldsymbol{B}_1$, while displacement currents (i.e., $i\omega\varepsilon_0\varepsilon_r\boldsymbol{E}$), induced by the permittivity of the sample, only introduce in-phase contributions to $\boldsymbol{B}_1$, and thus have no effect on the polarization of the field. The effect of conductivity is minimal at low fields, because the conduction currents induced in the sample are weak; therefore, the resulting out-of-phase contributions to $\boldsymbol{B}_1$ are small. As the field strength increases, these contributions become more significant and cause larger asymmetries in the spatial distribution of the right (Fig. 7) and left (results not shown) circularly polarized components of $\boldsymbol{B}_1$. A uniform phase distribution along the axis of the coil, almost unaffected by the presence of the sample, is observed at low frequencies [Fig. 7(E)], because associated wavelengths are large as compared to the sample size. Phase variations along the direction of the central axis of the coil increase with frequency as the wavelength becomes shorter and the conductive sample affects the propagation of the field. For example, the phase variation across the sample travelling away from the coil in Fig. 7(H) corresponds to approximately two and a half cycles, which is consistent with the ~12 cm

Author Manuscript Author Manuscript Author Manuscript Author Manuscript

wavelength within the sample (diameter = 30.6 cm) at 7 T. Additionally, at high field strengths, a prominent amplitude null is present between the large and small lobe of the transmit or the receive field pattern [Fig. 7(D)], and is coincident with the discontinuity observed off center from the axis of the coil in the corresponding phase image [Fig. 7(H)]. The null is due to perfect circular polarization in the opposite direction at that location. For example, in a $|B_1^+$ map, which contains only the right circularly polarized component (assuming $\boldsymbol{B}_0$ is oriented along negative z), the null corresponds to regions of primarily left circularly polarized fields. The ratio maps (either $|\boldsymbol{B}_1{}^+|$ or $|B_1^-$ divided by $\|\boldsymbol{B}_{1xy}\|$) in Fig. 9 further demonstrate that regions with large-amplitude right circularly polarized component correspond to low-amplitude left circularly polarized component and vice versa. Although the current distribution in a coil conductor is also increasingly asymmetric at higher field strengths (40), the consequent effects on the fields are unaccounted for in our results as our simulation framework assumes uniform current distribution throughout the coil.

An understanding of the effects of conductivity and permittivity on $\boldsymbol{B}_1$ field behavior is also at the root of certain recently developed electrical property mapping techniques, which may have potential for diagnostic imaging and local SAR prediction. Examples include MR Electrical Properties Tomography (MR-EPT), which uses measurements of the curvature of the $\boldsymbol{B}_1$ field in a body to estimate electrical properties under certain symmetry assumptions (41,42), and the more general Local Maxwell Tomography (LMT), which effectively inverts the Maxwell's equations to find the relative permittivity and conductivity without symmetry assumptions (43). Such RF-field-based methods complement prior surface-measurement-based electrical property mapping approaches such as Electrical Impedance Tomography (EIT) (44,45).

The main effect of a sample's permittivity is to change the wavelength of $\boldsymbol{B}_1$ within the sample (Eq. [16]) at a given frequency. Complex interference patterns arise in $|B_1^+$ (and similarly in $|B_1^-$) for low-conductivity samples when the permittivity is sufficiently high to shorten the wavelength considerably with respect to the dimensions of the sample (Fig. 8) (11–13). However, for a single surface coil, such patterns are seldom observed in vivo due to tissue conductivity and the complexity of tissue boundaries (2,3), which prevent the elaborate patterns seen in uniform phantoms. Interference patterns are not typically observed in oil phantoms or in fat tissue where both the conductivity (σ = 0.040 S/m at 297 MHz) and the relative permittivity (ε_r = 5.6 at 297 MHz) are low (34); therefore, the wavelength of $\boldsymbol{B}_1$ in the sample, in such situations, is typically longer than the size of the sample.

In previous studies, the receive field has been defined with (23) or without (28,46) the conjugate sign. While the amplitude is the same for both definitions, the phase distribution changes (see Appendix and Fig. 6). The difference in definitions is related to whether, conceptually, the coil is seen as the source of the field (as in simulation) or the sample is seen as the source of the signal (as in the experiment).

This work has focused on the effects of the operating MR frequency and sample electrical properties on the spatial distribution of $\boldsymbol{B}_1$ within the object. Note, however, that object size, coil structure and the polarization of the current drive scheme also contribute to the spatial

Author Manuscript Author Manuscript Author Manuscript Author Manuscript

distribution of $\boldsymbol{B}_1$. For example, the twisting asymmetry of $|B_1^+$ or $|B_1^-$ in a conductive sample at high field is not as strong for an electric dipole antenna as for a loop coil, because the induced magnetic field within the sample and the field generated by the dipole antenna cannot as effectively create a circularly polarized field. By applying an effective mirror current construct like that in Fig. 10 to an electric dipole, it can be appreciated that although the field created by the driving current and the field induced in a conductive sample have a 90 degree difference in phase, they are not oriented orthogonally (33).

Understanding the factors that determine $\boldsymbol{B}_1$ field patterns can benefit a number of MR applications, guide RF coil design, and aid in the development of methods to improve RF homogeneity at ultra high field strength. For example, knowledge of the asymmetry between $|B_1^+$ and $|B_1^-$ has been used to optimize the design of transmit-receive coil arrays (47–49). Recent work has shown that placing high permittivity materials near the object surface enhances and passively shims the $\boldsymbol{B}_1$ field inside the sample by exploiting displacement currents generated by the RF coil in the high permittivity material (50–53). Explaining these effects with a consistent theoretical framework is likely to become increasingly important for various applications in MRI.

CONCLUSIONS

We present a framework for understanding the dependence of the $\boldsymbol{B}_1$ spatial field patterns on the operating MR frequency and the electrical properties of the sample. While magnetic field pattern behavior in MRI has been reported previously in the literature, this article provides a unified framework for explaining the observed phenomena by examining Maxwell's equations, changes in polarized components of the field and wave propagation effects. In particular, we show that sample conductivity, rather than permittivity, is responsible for changing the $\boldsymbol{B}_1$ field polarization, and the consequent distribution of B_1^+ or B_1^- fields, causing the characteristic asymmetries observed in $|B_1^+$ and $|B_1^-$ maps, which are more pronounced at high field. On the other hand, elaborate interference patterns can appear in high permittivity samples, due to the inverse relationship between permittivity and wavelength, if conductivity is negligible. More highly conductive samples attenuate propagating waves and prevent the formation of intricate interference patterns. We expect that a thorough understanding of field pattern behavior will be useful for RF coil design, the application of high permittivity materials in MRI, and the development of new strategies to overcome RF inhomogeneities at ultra-high field strength.

Acknowledgments

This work was supported in part by NIH R01 EB002568, NIH R01 EB011551, NIH R01 EB000447, NSF 1453675 and was performed under the rubric of the Center for Advanced Imaging Innovation and Research (CAI2R, www.cai2r.net), a NIBIB Biomedical Technology Resource Center (NIH P41 EB017183). The authors thank Pippa Storey and Cem M. Deniz for helpful discussions regarding B_1 mapping techniques and Leeor Alon for discussions regarding algorithms for unwrapping phase images.

Author Manuscript Author Manuscript Author Manuscript Author Manuscript

APPENDIX

ALTERNATIVE DEFINITIONS OF B1− AND THEIR IMPLICATIONS FOR THE AMPLITUDE AND PHASE OF THE RECEIVE FIELD

The receive sensitivity distribution (otherwise known as the "receive field") has been defined in the MR literature with (23) and without (28,46) a conjugate sign. The difference in definitions is related to whether, conceptually, the coil is the source of the field (as in the simulation) or the sample is the source of the signal (as in the experiment). By substituting Eqs. [8] and [9] into these two definitions, the following equations show that while the amplitude is identical for both cases (Eqs. [A.1] and [A.2]), the phase differs (Eqs. [A.3] and [A.4]). Note that the phase of B_1^- and B_1^+ given by Eqs. [A.3] and [A.5] are equivalent if propagation-related and sample-induced phase changes are negligible (i.e., α and β both approach zero) and if the imposed phase ϕ reverses sign [Figs. 6(D,E)].

$$\left|\frac{(B_{1x}-iB_{1y})^*}{2}\right| = \frac{KI_0}{2}\sqrt{(C_{\mathrm{ox}}\ \cos(\phi+\alpha)+C_{\mathrm{oy}}\sin(\phi+\beta))^2+(-C_{\mathrm{ox}}\sin(\phi+\alpha)+C_{\mathrm{oy}}\cos(\phi+\beta))^2} \quad [A.1]$$

$$\left|\frac{(B_{1x}-iB_{1y})}{2}\right| = \frac{KI_0}{2}\sqrt{(C_{ox}\ \cos(\phi+\alpha)+C_{oy}\sin(\phi+\beta))^2+(+C_{ox}\sin(\phi+\alpha)-C_{oy}\cos(\phi+\beta))^2} \quad [A.2]$$

$$\angle\frac{(B_{1x}-iB_{1y})^*}{2} = \arctan\left(\frac{KI_0}{2}\left(\frac{-C_{ox}\sin(\phi+\alpha)+C_{oy}\cos(\phi+\beta)}{C_{ox}\cos(\phi+\alpha)+C_{oy}\sin(\phi+\beta)}\right)\right) \quad [A.3]$$

$$\angle\frac{(B_{1x}-iB_{1y})}{2} = \arctan\left(\frac{KI_0}{2}\left(\frac{+C_{\mathrm{ox}}\sin(\phi+\alpha)-C_{\mathrm{oy}}\cos(\phi+\beta)}{C_{\mathrm{ox}}\cos(\phi+\alpha)+C_{\mathrm{oy}}\sin(\phi+\beta)}\right)\right) \quad [A.4]$$

$$\angle\frac{(B_{1x}+iB_{1y})}{2} = \arctan\left(\frac{KI_0}{2}\left(\frac{+C_{\mathrm{ox}}\sin(\phi+\alpha)+C_{\mathrm{oy}}\cos(\phi+\beta)}{C_{\mathrm{ox}}\cos(\phi+\alpha)-C_{\mathrm{oy}}\sin(\phi+\beta)}\right)\right) \quad [A.5]$$

Author Manuscript Author Manuscript Author Manuscript Author Manuscript

REFERENCES

1. Glover GH, Hayes CE, Pelc NJ, Edelstein WA, Mueller OM, Hart HR, et al. Comparison of linear and circular-polarization for magnetic-resonance imaging. J Magn Reson Imaging. 1985; 64:255–270.
2. Bomsdorf H, Helzel T, Kunz D, Röschmann P, Tschendel O, Wieland J. Spectroscopy and imaging with a 4 tesla whole-body MR system. NMR Biomed. 1988; 1:151–158. [PubMed: 3275125]
3. Kangarlu A, Baertlein BA, Lee R, Ibrahim T, Yang L, Abduljalil AM, et al. Dielectric resonance phenomena in ultra high field MRI. J Comput Assist Tomogr. 1999; 23:821–831. [PubMed: 10589554]
4. Hoult DI. Sensitivity and power deposition in a high-field imaging experiment. J Magn Reson Imaging. 2000; 12:46–67. [PubMed: 10931564]
5. Tropp J. Image brightening in samples of high dielectric constant. J Magn Reson Imaging. 2004; 167:12–24.
6. Sled JG, Pike GB. Standing-wave and RF penetration artifacts caused by elliptic geometry: an electrodynamic analysis of MRI. IEEE Trans Med Imaging. 1998; 17:653–662. [PubMed: 9845320]
7. Ibrahim TS, Lee R, Abduljalil AM, Baertlein BA, Robitaille P-ML. Dielectric resonances and B1 field inhomogeneity in UHFMRI: computational analysis and experimental findings. Magn Reson Imaging. 2001; 19:219–226. [PubMed: 11358660]
8. Wardenier, PH. 8th Annual Meeting and Exhibition. Amsterdam: Society of Magnetic Resonance in Medicine; 1989. Local intensity shift artifact (LISA); p. 1175
9. Keltner JR, Carlson JW, Roos MS, Wong ST, Wong TL, Budinger TF. Electromagnetic fields of surface coil in vivo NMR at high frequencies. Magn Reson Med. 1991; 22:467–480. [PubMed: 1812380]
10. Barfuss H, Fischer H, Hentschel D, Ladebeck R, Oppelt A, Wittig R, et al. In vivo magnetic resonance imaging and spectroscopy of humans with a 4 t whole-body magnet. NMR Biomed. 1990; 3:31–45. [PubMed: 2390452]
11. Tofts PS. Standing waves in uniform water phantoms. J Magn Reson Ser B. 1994; 104:143–147.
12. Yang QX, Wang J, Zhang X, Collins CM, Smith MB, Liu H, et al. Analysis of wave behavior in lossy dielectric samples at high field. Magn Reson Med. 2002; 47:982–989. [PubMed: 11979578]
13. Collins CM, Liu W, Schreiber W, Yang QX, Smith MB. Central brightening due to constructive interference with, without, and despite dielectric resonance. J Magn Reson Imaging. 2005; 21:192–196. [PubMed: 15666397]
14. Van de Moortele P-F, Akgun C, Adriany G, Moeller S, Ritter J, Collins CM. B1 destructive interferences and spatial phase patterns at 7 T with a head transceiver array coil. Magn Reson Med. 1989; 54:1503–1518. 2005.
15. Vaughan JT, Garwood M, Collins CM, Liu W, DelaBarre L, Adriany G, et al. 7T vs. 4T: RF power, homogeneity, and signal-to-noise comparison in head images. Magn Reson Med. 2001; 46:24–30. [PubMed: 11443707]
16. Vaughan JT, Snyder CJ, DelaBarre LJ, Bolan PJ, Tian J, Bolinger L, et al. Whole-body imaging at 7T: preliminary results. Magn Reson Med. 2009; 61:244–248. [PubMed: 19097214]
17. Ibrahim TS, Lee R, Baertlein BA, Abduljalil AM, Zhu H, Robitaille P-ML. Effect of RF coil excitation on field inhomogeneity at ultra high fields: a field optimized TEM resonator. Magn Reson Imaging. 2001; 19:1339–1347. [PubMed: 11804762]
18. Metzger GJ, Snyder C, Akgun C, Vaughan T, Ugurbil K, Van de Moortele PF. Local B1+ shimming for prostate imaging with transceiver arrays at 7T based on subject-dependent transmit phase measurements. Magn Reson Med. 2008; 59:396–409. [PubMed: 18228604]
19. Katscher U, Bornert P, Leussler C, van den Brink JS. Transmit SENSE. Magn Reson Med. 2003; 49:144–150. [PubMed: 12509830]
20. Zhu Y. Parallel excitation with an array of transmit coils. Magn Reson Med. 2004; 51:775–784. [PubMed: 15065251]

Author Manuscript Author Manuscript Author Manuscript Author Manuscript

21. Lattanzi R, Sodickson DK, Grant AK, Zhu Y. Electrodynamic constraints on homogeneity and radiofrequency power deposition in multiple coil excitations. Magn Reson Med. 2009; 61:315–334. [PubMed: 19165885]
22. Hoult DI, Chen CN, Sank VJ. Quadrature detection in the laboratory frame. Magn Reson Med. 1984; 1:339–353. [PubMed: 6571563]
23. Hoult DI. The principle of reciprocity in signal strength calculations - a mathematical guide. Concept Magn Res. 2000; 12:173–187.
24. Ibrahim TS, Mitchell C, Abraham R, Schmalbrock P. In-depth study of the electromagnetics of ultrahigh-field MRI. NMR Biomed. 2007; 20:58–68. [PubMed: 17006885]
25. Vaidya, MV.; Sodickson, DK.; Brown, R.; Wiggins, GC.; Lattanzi, R. B1+ and B1− field pattern dependence on the electrical properties of the sample and the static magnetic field strength. Proceedings of the 20th Annual Meeting of ISMRM; May 2012; Melbourne. 2012. p. 2796
26. Stollberger, R.; Wach, P. The generalized principle of reciprocity in NMR experiments with conductive objects. 8th Annual Meeting and Exhibition, Society of Magnetic Resonance in Medicine; August 1989; Amsterdam. 1989. p. 1174
27. Collins CM, Wang Z. Calculation of radiofrequency electromagnetic fields and their effects in MRI of human subjects. Magn Reson Med. 2011; 65:1470–1482. [PubMed: 21381106]
28. Ibrahim TS. Analytical approach to the MR signal. Magn Reson Med. 2005; 54:677–682. [PubMed: 16088924]
29. Tropp J. Reciprocity and gyrotropism in magnetic resonance transduction. Phys Rev A. 2006; 74:062103.
30. Lattanzi R, Sodickson DK. Ideal current patterns yielding optimal signal-to-noise ratio and specific absorption rate in magnetic resonance imaging: computational methods and physical insights. Magn Reson Med. 2012; 68:286–304. [PubMed: 22127735]
31. Johnk, CTA. Engineering Electromagnetic Fields and Waves. 2nd. New York: John Wiley and Sons; 1988. p. 103-157.
32. Collins CM, Yang QX, Wang JH, Zhang X, Liu H, Michaeli S, et al. Different excitation and reception distributions with a single-loop transmit-receive surface coil near a head-sized spherical phantom at 300 MHz. Magn Reson Med. 2002; 47:1026–1028. [PubMed: 11979585]
33. Zhang, B.; Sodickson, DK.; Lattanzi, R.; Wiggins, GC. Why does the Radiative Antenna Have no B1 Twisting at 7T? Framework for and applications of a conceptual “mirror current” model of coil-tissue interactions. Proceedings of the 20th Annual Meeting of ISMRM; May 2012; Melbourne. 2012. p. 2816
34. Gabriel S, Lau RW, Gabriel C. The dielectric properties of biological tissues: II. Measurements in the frequency range 10 Hz to 20 GHz. Phys Med Biol. 1996; 41:2251. [PubMed: 8938025]
35. Klose U. Mapping of the radio frequency magnetic field with a MR snapshot FLASH technique. Med Phys. 1992; 19:1099–1104. [PubMed: 1518473]
36. Goldstein RM, Zebken HA, Werner CL. Satellite radar interferometry: two-dimensional phase unwrapping. Radiol Sci. 1988; 23:713–720.
37. Ghiglia, DC.; Pritt, MD. Two-Dimensional Phase Unwrapping: Theory, Algorithms and Software. New York: Wiley-Interscience; 1998.
38. Schnell W, Renz W, Vester M, Ermert H. Ultimate signal-to-noise-ratio of surface and body antennas for magnetic resonance imaging. IEEE Trans Antennas Propag. 2000; 48:418–428.
39. Hoult D, Richards R. The signal-to-noise ratio of the nuclear magnetic resonance experiment. J Magn Reson Imaging. 1976; 24:71–85.
40. Rautio JC. An investigation of microstrip conductor loss. Microwave Magazine IEEE. 2000; 1:60–67.
41. Katscher U, Voigt T, Findeklee C, Vernickel P, Nehrke K, Dossel O. Determination of electric conductivity and local SAR via B1 mapping. Med Imaging IEEE Trans. 2009; 28:1365–1374.
42. Katscher U, Kim D-H, Seo JK. Recent progress and future challenges in MR electric properties tomography. Comput Math Methods Med. 2013; 2013:11.
43. Sodickson, DK.; Alon, L.; Deniz, CM.; Brown, R.; Zhang, B.; Wiggins, GC., et al. Local maxwell tomography using transmit-receive coil arrays for contact-free mapping of tissue electrical

Author Manuscript Author Manuscript Author Manuscript Author Manuscript

properties and determination of absolute RF phase. Proceedings of the 20th Annual Meeting of ISMRM; May 2012; Melbourne. 2012. p. 387

44. Newell JC, Gisser DG, Isaacson D. An electric current tomography. Biomed Eng IEEE Trans. 1988; 35:828–833.
45. Barber DC. A review of image reconstruction techniques for electrical impedance tomography. Med Phys. 1989; 16:162–169. [PubMed: 2654593]
46. Jackson. Classical Electrodynamics. New York: Wiley; 1999.
47. Wiggins, GC.; Zhang, B.; Duan, Q.; Lattanzi, R.; Biber, S.; Stoeckel, B., et al. 7 Tesla transmit-receive array for carotid imaging: simulation and experiment. Proceedings of the 17th Annual Meeting of ISMRM; April 2009; Hawaii. 2009. p. 393
48. Duan, Q.; Sodickson, DK.; Lattanzi, R.; Zhang, B.; Wiggins, GC. Optimizing 7T spine array design through offsetting of transmit and receive elements and quadrature excitations. Proceedings of the 18th Annual Meeting of ISMRM; May 2010; Stockholm. 2010. p. 51
49. Brown R, Deniz CM, Zhang B, Chang G, Sodickson DK, Wiggins GC. Design and application of combined 8-channel transmit and 10-channel receive arrays and radiofrequency shimming for 7-T shoulder magnetic resonance imaging. Investigative Radiol. 2014; 49:35–47.
50. Webb AG. Dielectric materials in magnetic resonance. Concepts Magn Reson Part A. 2011; 38:148–184.
51. Yang QX, Rupprecht S, Luo W, Sica C, Herse Z, Wang J, et al. Radiofrequency field enhancement with high dielectric constant (HDC) pads in a receive array coil at 3.0T. J Magn Reson Imaging. 2013
52. Yang QX, Mao W, Wang J, Smith MB, Lei H, Zhang X, et al. Manipulation of image intensity distribution at 7.0 T: passive RF shimming and focusing with dielectric materials. J Magn Reson Imaging. 2006; 24:197–202. [PubMed: 16755543]
53. Vaidya, MV.; Oh, S.; Collins, CM.; Sodickson, DK.; Lattanzi, R. Manipulating B1 spatial distribution at 7 Tesla with dielectric pads at a distance from a transmit surface coil. Proceedings of the 21th Annual Meeting of ISMRM; April 2013; Salt Lake City. 2013. p. 4379

Author Manuscript Author Manuscript Author Manuscript Author Manuscript

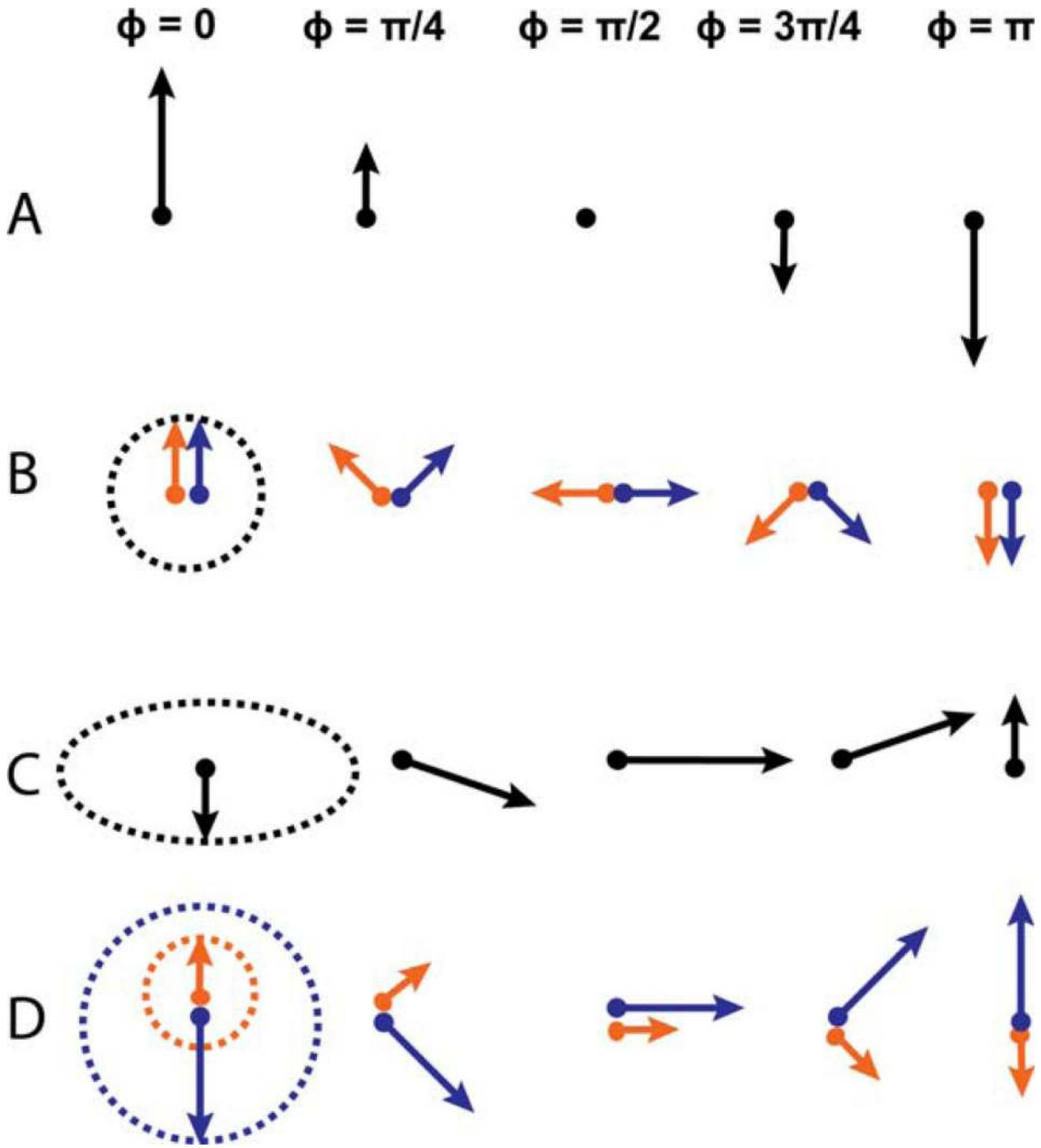

Figure 1.

Schematic showing how linearly (A) and elliptically (C) polarized vectors can be decomposed into two circularly polarized vectors (B and D, respectively). B shows the phase evolution for two equal counter-rotating vectors (orange and blue arrows). The vector sum of these circularly polarized vectors is equal to the linearly polarized vector in A (black arrows). Two unequal counter-rotating circularly polarized vectors, a larger right circularly polarized (counter-clockwise) vector in blue and a smaller left circularly polarized

(clockwise) vector in orange, are shown D. The vector sum of these two vectors is equal to the elliptically polarized vector shown in C.

Author Manuscript Author Manuscript Author Manuscript Author Manuscript

Author Manuscript Author Manuscript Author Manuscript Author Manuscript

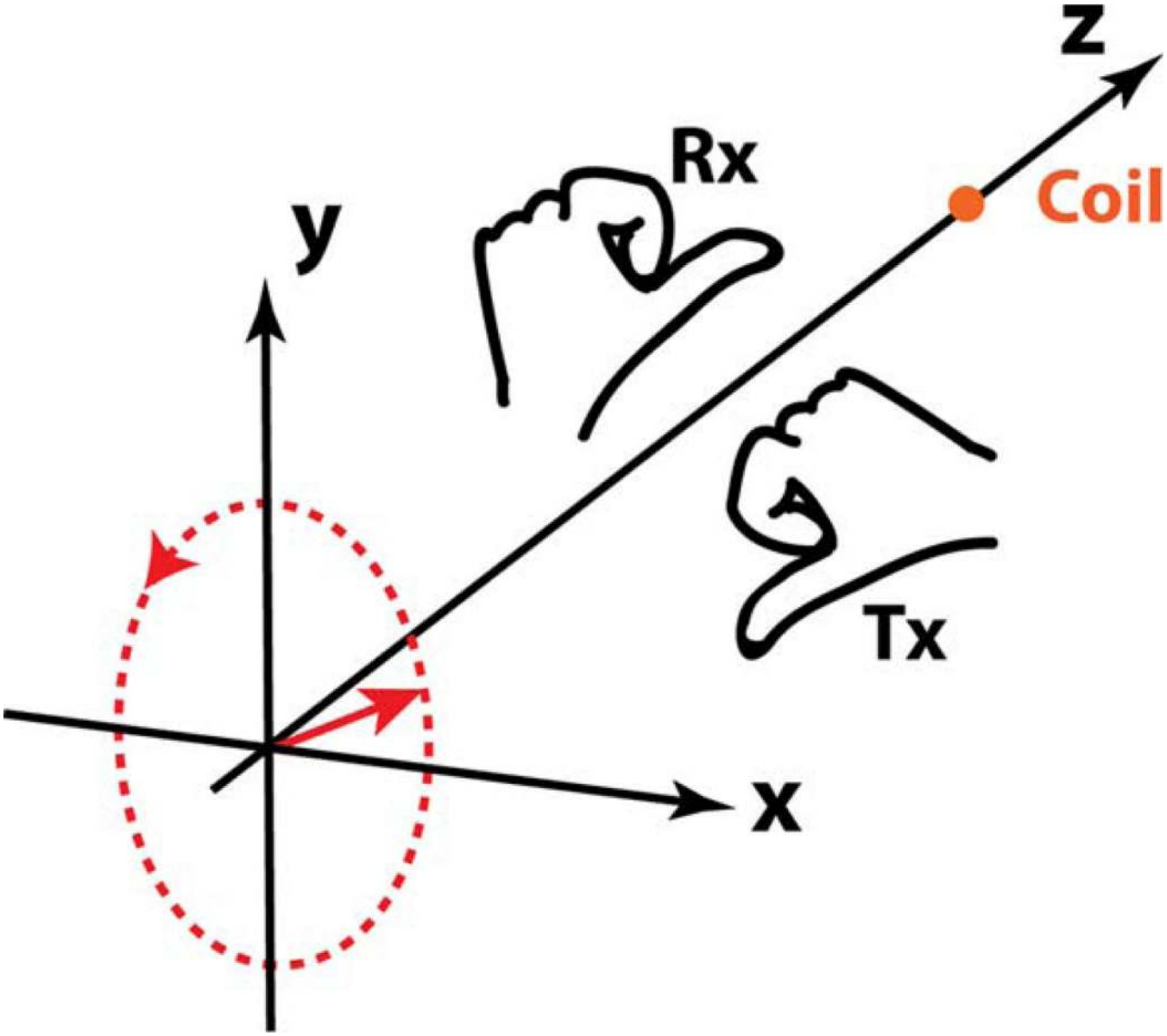

Figure 2.

Intuitive illustration of the opposite polarizations of transmit (Tx) and receive (Rx) fields. During transmission, the $\boldsymbol{B}_1$ field propagates from the coil to the spin (red), as shown by the thumb of the right hand, whose fingers curl in the direction of precession. During reception the $\boldsymbol{B}_1$ field propagates from the spin to the coil, which is the direction indicated by the thumb of a left hand, whose fingers also curl in the direction of precession. It may be proven mathematically by applying the principle of reciprocity (23) that the sensitivity distribution of a receive coil shares the handedness of what we have identified in the theory section as the "receive field," i.e., it has a polarization opposite to that of the transmit field. Note that depending on the position of the sample with respect to the coil and the direction of the $\boldsymbol{B}_0$ field, the handedness of the two fields may be interchanged, but will always be opposite to one other.

Author Manuscript Author Manuscript Author Manuscript Author Manuscript

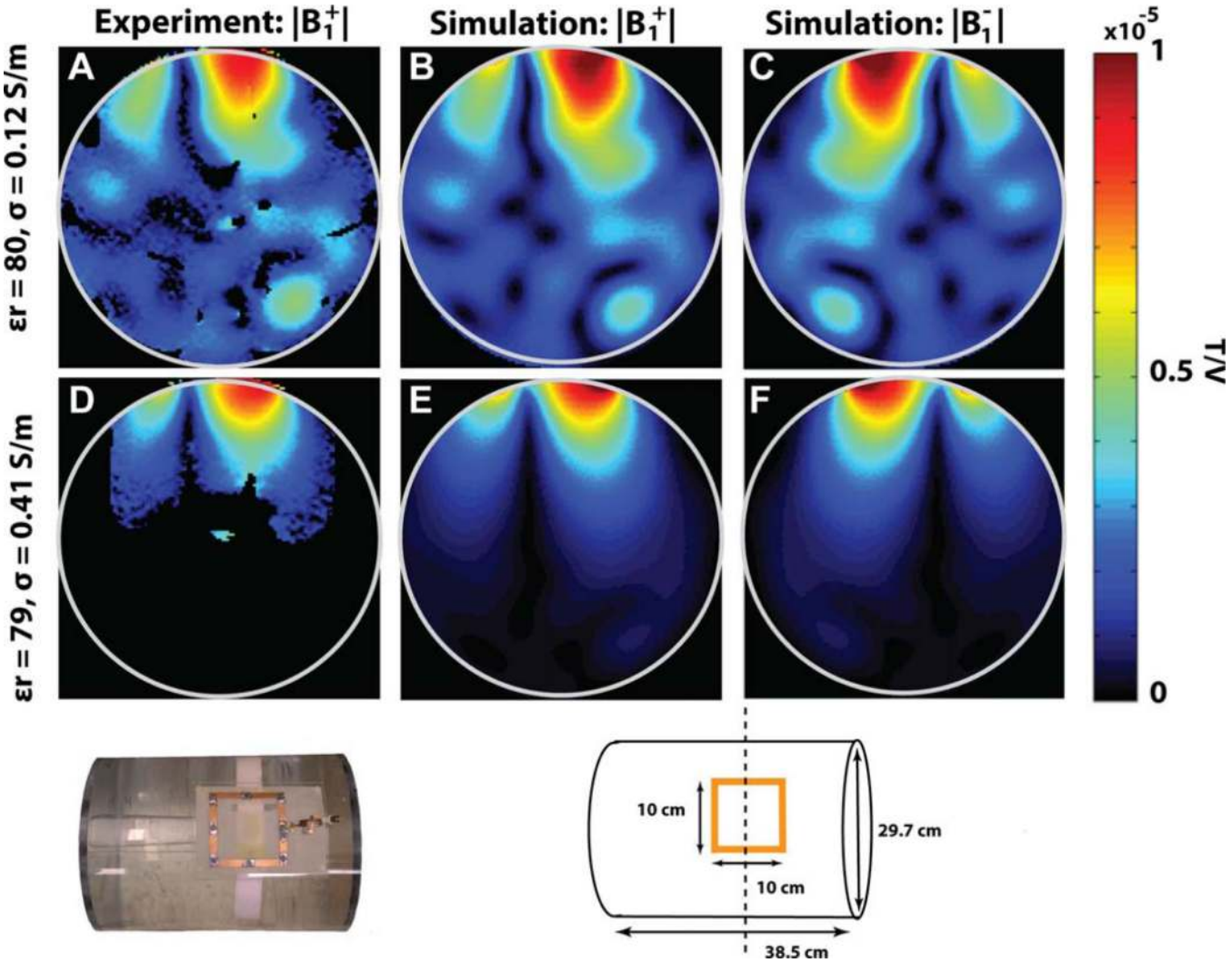

Figure 3.

The effect of sample conductivity is shown in experimental and simulated B_1 maps at 7 T. Experimental and simulation set-up are shown in the bottom row. Transmit (B_1^+) and receive (B_1^-) fields were calculated for a transverse plane through the center of the coil as shown by the dotted line. For low sample conductivity (A, B) the wavelength (λ = 11.31 cm) is shorter than the diameter of the phantom, and the skin depth (δ = 38.71 cm) is much longer than the phantom diameter, allowing forward and reflected waves to create an interference pattern. For a sample with larger conductivity (D, E), the wavelength is comparable (λ = 11.24 cm), since $\varepsilon_r\varepsilon_0\omega \gg \sigma$, whereas the skin depth (δ = 11.62 cm) is much shorter and attenuates the forward wave, preventing the occurrence of interference patterns. Note that some nulls in the experimental flip angle map (A) are artifacts due to lack of receive signal as seen in the simulated $|B_1^-$ map (C). Note also that the simulated $|B_1^+$ and $|B_1^-$ maps are mirror images of each other. Experimental results match well with simulation results (A, D vs. B, E).

Author Manuscript Author Manuscript Author Manuscript Author Manuscript

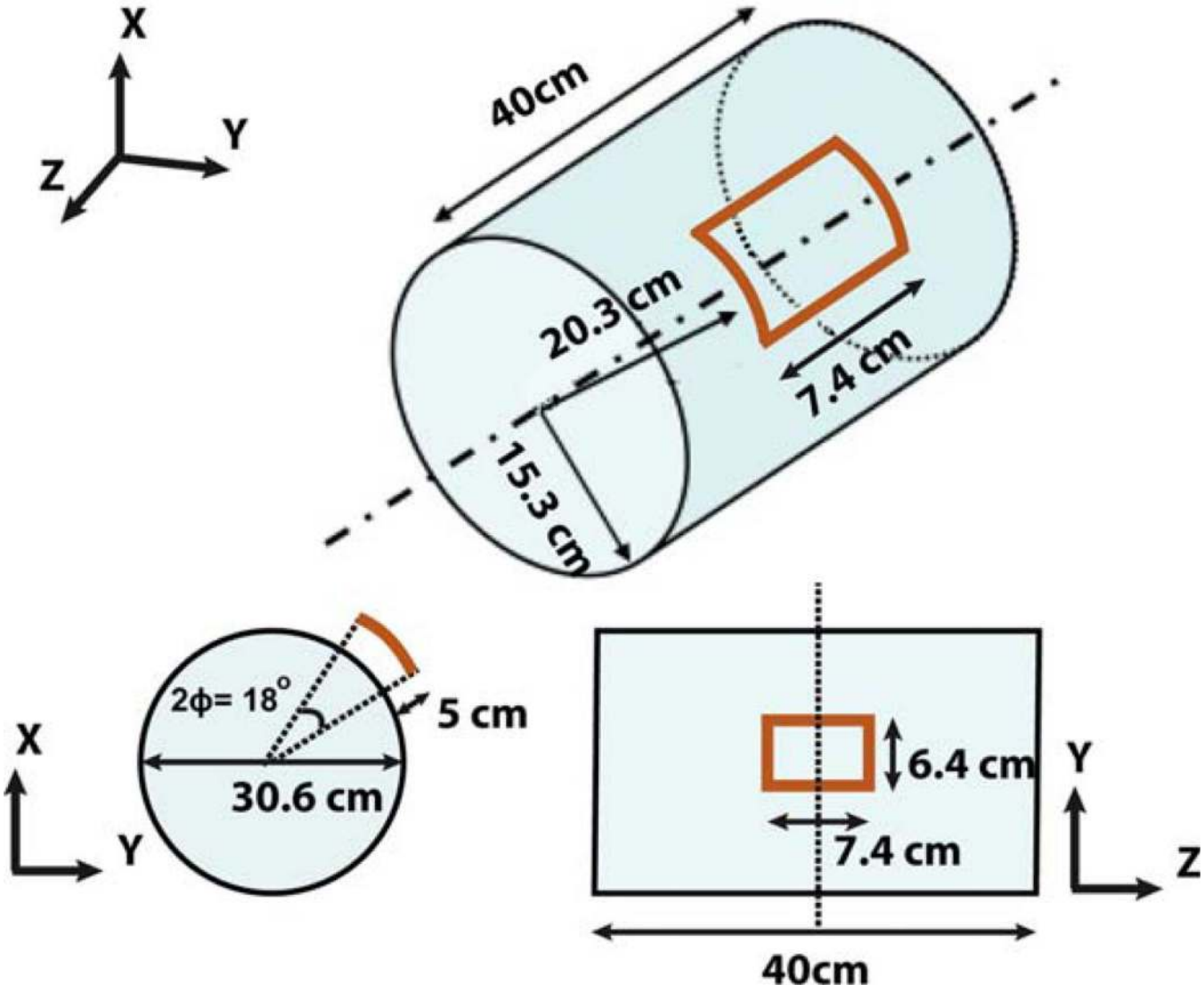

Figure 4.

Phantom and coil geometry for DGF simulations in Figs. 5 to 9. The EM field associated with the coil (in orange) was calculated for the transverse plane through the center of the coil shown by the dotted line in the Y–Z plane. The shape of the coil is a cylindrical window that follows the curvature of the object.

Author Manuscript Author Manuscript Author Manuscript Author Manuscript

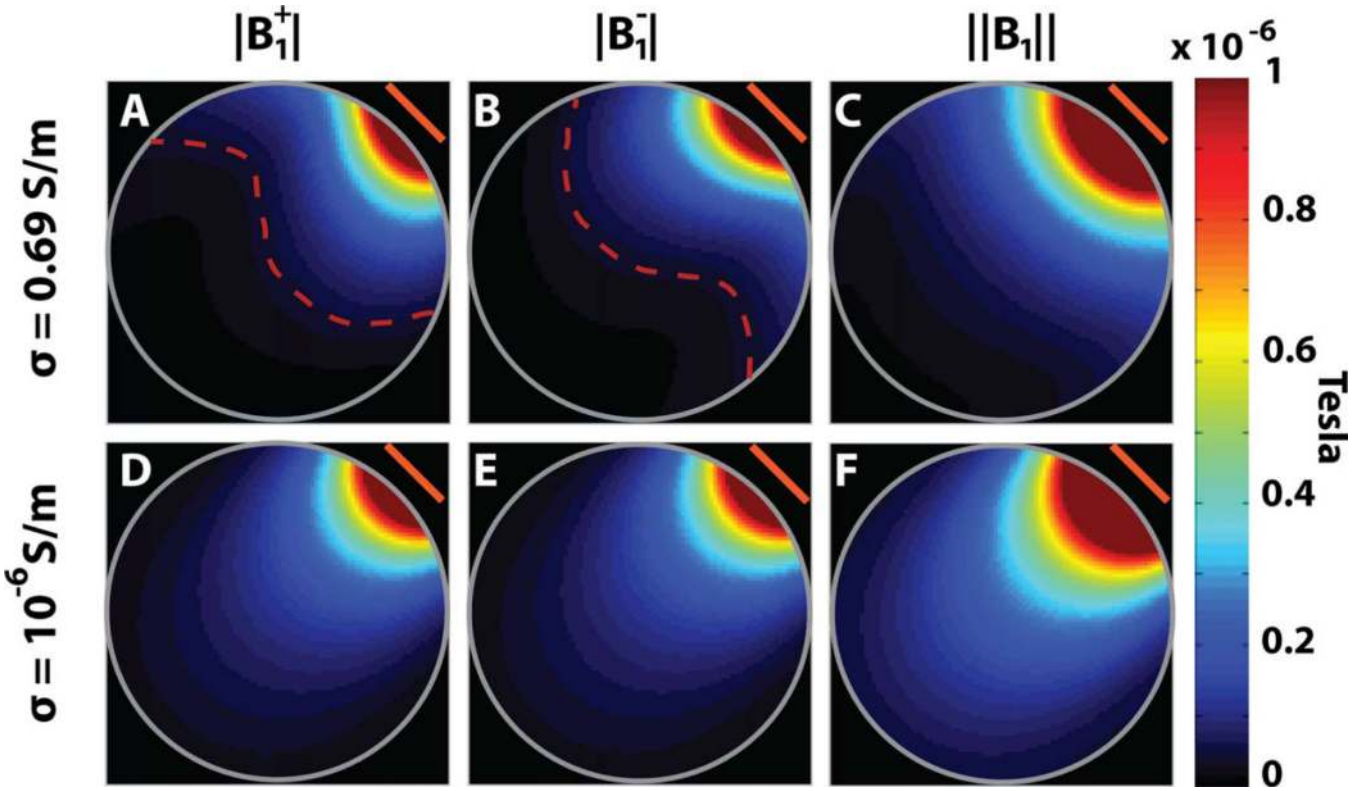

Figure 5.

Effect of electrical conductivity on $|B_1^+|$, $|B_1^-|$ and $\|\boldsymbol{B}_1\|$ at 1.5 T (simulation results). For a conductive sample (top row) with $\varepsilon_r = 79$ and $\sigma = 0.69$ S/m, $|B_1{}^+|$ (A) and $|B_1^-$ (B) are asymmetric and twist in opposite directions (red dashed lines). For a nonconductive sample ($\varepsilon_r = 79$ and $\sigma = 10^{-6}$ S/m), $|B_1^+$ (D) and $|B_1^-$ (E) are equal and symmetric with respect to the coil position (orange line). The spatial distribution of $\|\boldsymbol{B}_1\|$, which has both left and right circularly polarized contributions, is symmetric in both cases (C and F), but is attenuated in the conductive sample (C).

Author Manuscript Author Manuscript Author Manuscript Author Manuscript

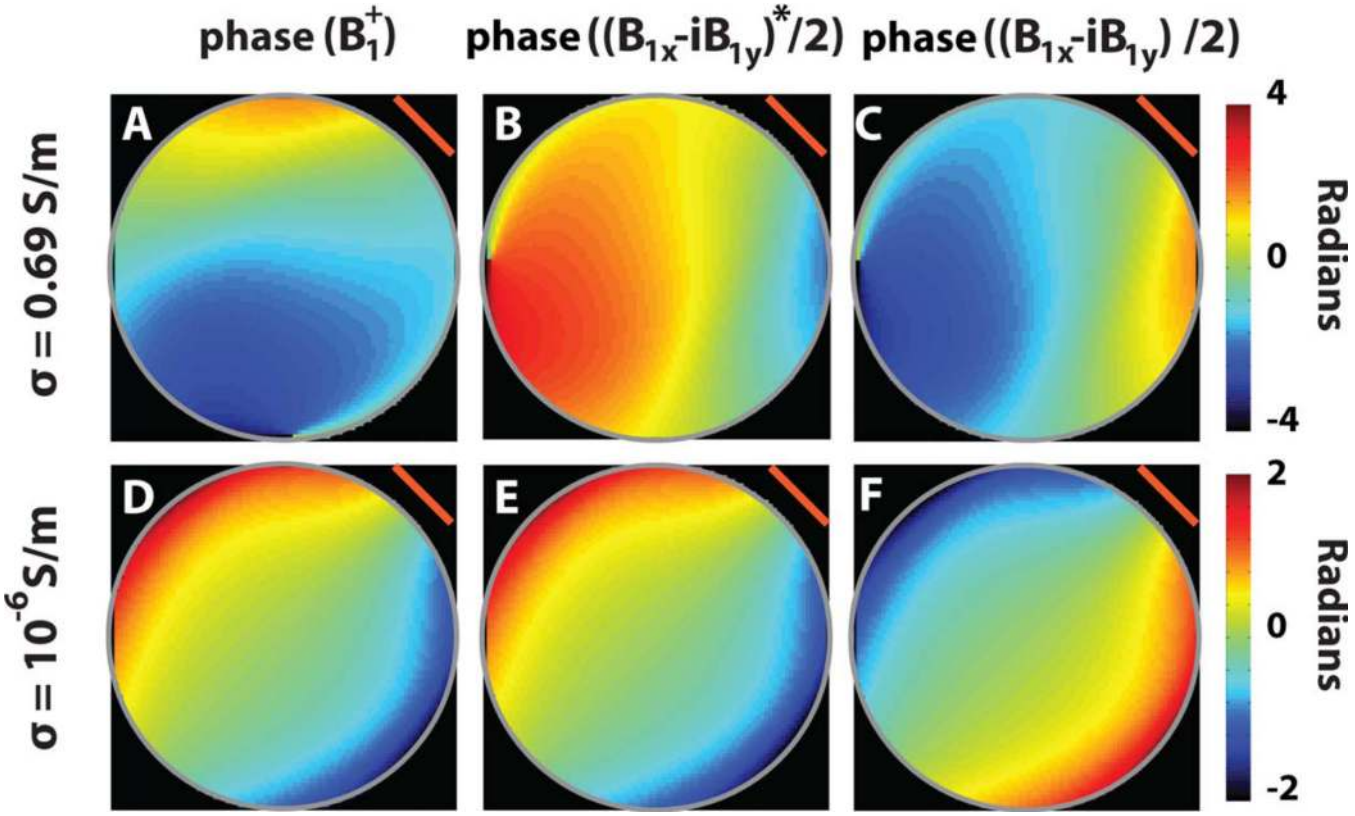

Figure 6.

Effect of electrical conductivity on the phase distribution of B_1^+ and B_1^- at 1.5 T (simulation results). For a sample with near zero conductivity ($\varepsilon_r = 79$ and $\sigma = 10^{-6}$ S/m, bottom row), the phase is approximately equal to that in the absence of the sample, with a constant value along the direction of the axis of the coil. For a conductive sample ($\varepsilon_r = 79$ and $\sigma = 0.69$ S/m, top row), conduction currents induced within the sample make the phase inhomogeneous with large variations at positions distant from the coil. The phase images differ for the two definitions of B_1^- that have been used in the MR literature (B vs. C and E vs. F). If B_1^- is defined without the conjugate sign, its phase distribution is a perfect mirror image of the phase distribution of B_1^+ with respect to the central axis of the coil (orange line) (A vs. C and D vs. F).). If B_1^- is defined with the conjugate sign, for a sample with low conductivity the phase images of B_1^+ and B_1^- are equal (D vs. E, see Appendix), but for a sample with high conductivity the apparent direction of phase evolution has locations far from the coil leading locations near the coil when the conjugate is present and the opposite when it is absent. This reflects the difference in whether the coil is considered the source of the field or the recipient of the signal produced in the sample.

Author Manuscript Author Manuscript Author Manuscript Author Manuscript

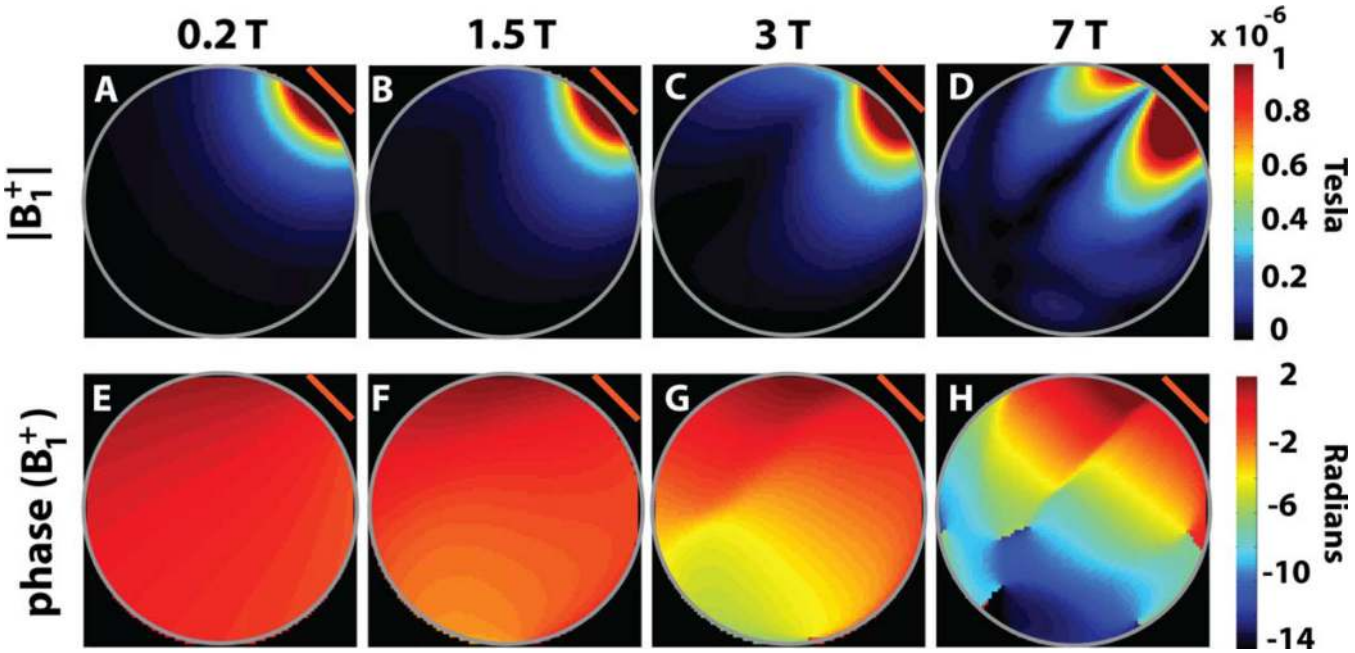

Figure 7.

Dependence of B_1^+ amplitude and phase on main magnetic field strength (simulation results). For a sample with $\varepsilon_r = 79$ and $\sigma = 0.5$ S/m, the asymmetry of the amplitude of the transmit field with respect to the center of the surface coil (orange line) increases with field strength due to larger conduction currents that induce larger out-of-phase contributions to the field (A–D). Corresponding phase images are shown in the bottom row (E–H). At low field, the phase distribution of B_1^+ inside the sample is relatively homogeneous, and at 0.2 T (E) is affected minimally by the presence of the sample. At high field, the wavelength is shorter than the object dimensions, and the phase of the transmit field at 7 T (H) varies considerably inside the sample, clearly reflecting the propagation of B_1^+ along the axis of the coil.

Author Manuscript Author Manuscript Author Manuscript Author Manuscript

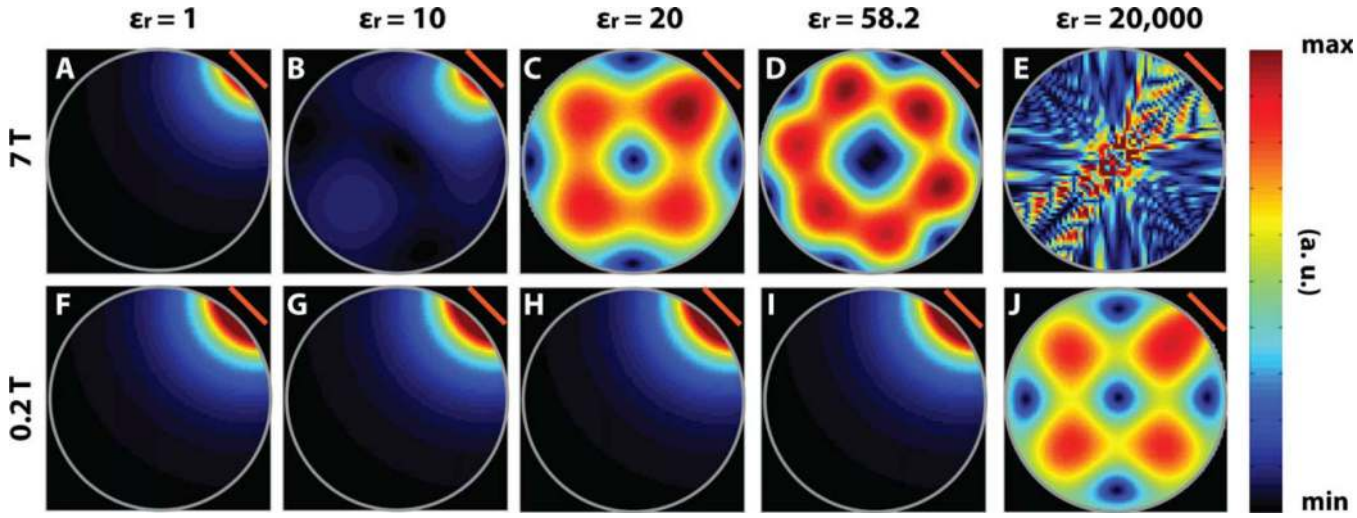

Figure 8.

Interference patterns in $|B_1^+$ for a nonconductive sample ($\sigma = 10^{-6}$ S/m) (simulation results). At 7 T, interference patterns become more pronounced (A–E) for increasing relative permittivity, as the wavelength becomes smaller compared to the object dimensions. At 0.2 T (F–J), on the other hand, the free-space wavelength ($\lambda = 35.3$ m for $\varepsilon_r = 1$, $\sigma = 0$) of the transmit field is considerably larger than the object, therefore it is only at extremely high values of relative permittivity (20,000 in (J)) that the wavelength becomes short enough to generate interference patterns. Note that the plots were scaled differently to account for differences in amplitude.

Author Manuscript Author Manuscript Author Manuscript Author Manuscript

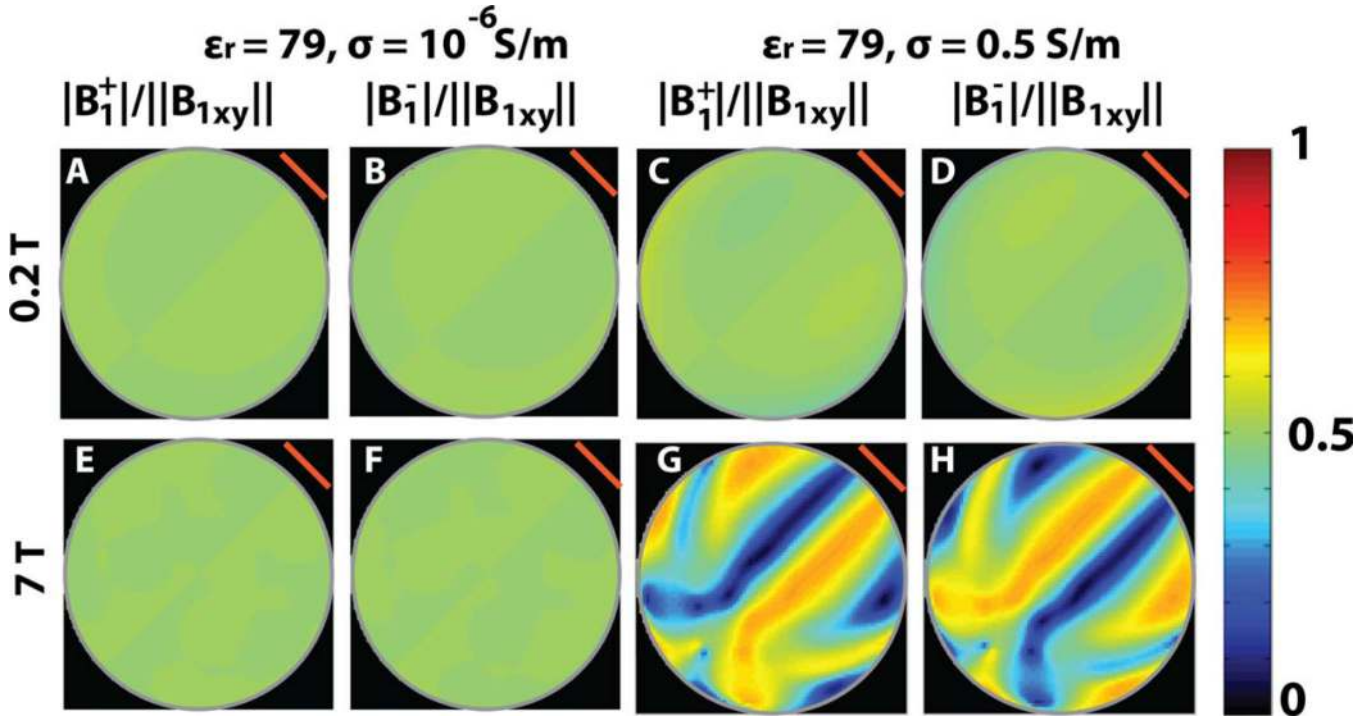

Figure 9.

Ratio of the amplitude of the coil's right $(|B_1^+|)$ and left $(|B_1^-|)$ circularly polarized magnetic fields as defined in Eq. [10] to the norm of the corresponding transverse field ($\|\boldsymbol{B}_{1xy}\|$) as defined in Eq. [5] (simulation results). For a nonconductive sample (A, B, E, F), both $|B_1^+$ and $|B_1^-$ are approximately half of $\|\boldsymbol{B}_{1xy}\|$ at both low and high field strength (see Eq. [11]). For a conductive sample, at low field (C, D) the same relationship holds, whereas at high field the distribution of both transmit (G) and receive (H) fields differs from that of $\|\boldsymbol{B}_{1xy}\|$, due to considerable phase changes caused by conduction currents induced within the object (see explanation following Eqs. [12] and [13]). In (G), regions with very high values in the map (close to 1, or red in the color bar) of right circularly polarized field components have very low values (close to 0, or dark blue in the color bar) in the map of left circularly polarized field components in figure H.

Author Manuscript Author Manuscript Author Manuscript Author Manuscript

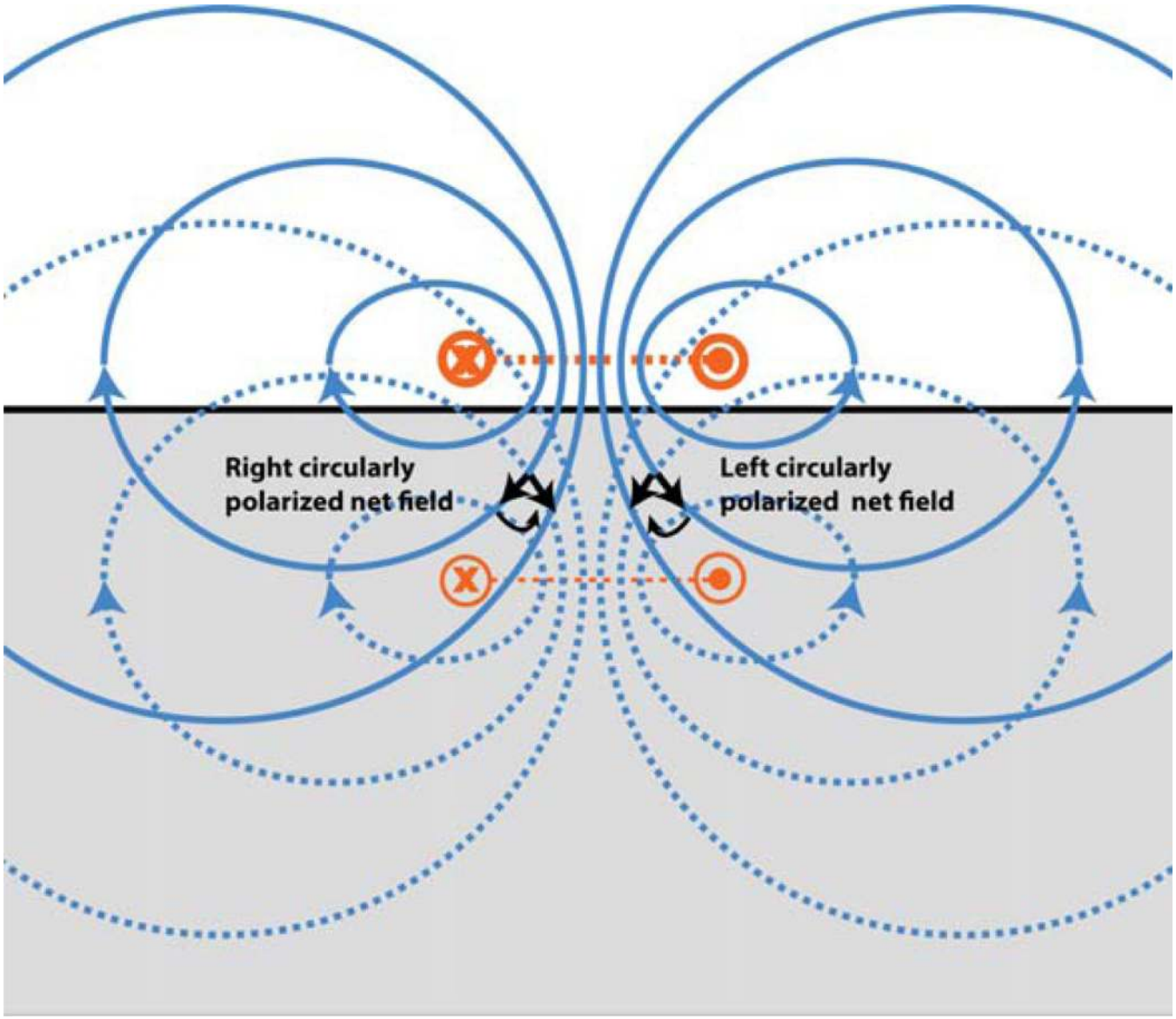

Figure 10.

Conceptual illustration of the mechanisms responsible for the generation of particular elliptical polarization patterns of RF magnetic field inside a conductive sample. For a coil (dark orange dotted line, "x" indicating current passing into the plane of the image, and "o" indicating current coming out of the plane) placed above a conductive sample (gray), the induced free-space magnetic field (as a consequence of the modified Ampere's Law) is shown in solid blue. This time-varying field then induces conduction currents or "eddy currents" in the sample. The approximate distribution of these eddy currents may be predicted using a simple effective "mirror current" construct, in which the sample conductivity is responsible for a partial "reflection" of the driving current. A simplified mirror current loop is depicted within the sample in light orange. This effective mirror current in turn induces its own magnetic field, shown by the dotted blue lines. The interacting magnetic field lines (solid and dotted blue) are out of phase (Faraday's law,

Author Manuscript Author Manuscript Author Manuscript Author Manuscript

modified Ampere's law) and are also spatially orthogonal in certain regions. As a result, right circular polarization predominates on one side of the coil, while left circular polarization predominates on the other side. This explains the asymmetries observed in $|B_1^+$ or $|B_1^-$ maps, since they show contributions of only right or only left circularly polarized component, respectively. Only regions that are primarily linearly polarized—for example, the region along the center of the coil—will contribute equally to transmit and receive field maps.